

Research Articles





How to cite: *Angew. Chem. Int. Ed.* **2021**, *60*, 13959–13968 International Edition: doi.org/10.1002/anie.202017031 German Edition: doi.org/10.1002/ange.202017031

Generating Assembled MFI Nanocrystals with Reduced b-Axis through Structure-Directing Agent Exchange Induced Recrystallization

Xiaoling Zhao⁺, Shu Zeng⁺, Xueliang Zhang, Quanzheng Deng, Xiujie Li, Wenguang Yu, Kake Zhu,* Shutao Xu,* Jichang Liu, and Lu Han*

Abstract: Controlling crystal size and shape of zeolitic materials is an effective way to promote their mass transport and catalytic properties. Herein, we report a single step, Na+and porogen- free crystallization of MFI hierarchical architecture made up of aligned nanocrystals with reduced b-axis thickness (5-23 nm) and adjustable Si/Al ratios between 35 to 120, employing the commonly used tetrapropylammonium hydroxide (TPAOH) and tetrabutylammonium hydroxide (TBAOH) as structure-directing agents (SDAs). Homogeneous nucleation driven by both SDAs and subsequent SDAexchange induced dissolution-recrystallization are responsible for the formation of such structure. The enhanced textural and diffusion properties account for a notable exaggeration of propene selectivity and catalyst lifetime in dimethyl ether-toolefins (DTO) conversion. This protocol is extendable to the rational synthesis of other hierarchical zeolites through crystallization process control.

Introduction

Zeolites are inorganic solids comprising of crystalline framework and penetrating micropores whose size is close to that of molecules, [1] showing broad applications as commer-

 $[^{\star}] \,$ X. Zhao, $^{[+]}$ Prof. K. Zhu, Prof. J. Liu

UNILAB, State Key Laboratory of Chemical Engineering East China University of Science and Technology

Shanghai 200237 (P. R. China)

E-mail: kakezhu@ecust.edu.cn

S. Zeng,[+] Prof. X. Li, Prof. W. Yu, Prof. S. Xu

National Engineering Laboratory for Methanol to Olefins

Dalian National Laboratory for Clean Energy

Dalian Institute of Chemical Physics

Chinese Academy of Sciences, Dalian 116023 (P. R. China)

E-mail: xushutao@dicp.ac.cn

X. Zhang, Q. Deng, Prof. L. Han

School of Chemical Science and Engineering, Tongji University

Shanghai, 200092 (P. R. China)

E-mail: luhan@tongji.edu.cn

S. Zeng^[+]

University of Chinese Academy of Sciences

Beijing 100049 (China)

X. Zhang

School of Chemical and Chemical Engineering Shanghai Jiao Tong University, Shanghai 200024 (China)

[+] These authors contributed equally to this work.

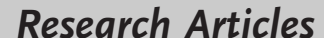
Supporting information and the ORCID identification number(s) for

the author(s) of this article can be found under: https://doi.org/10.1002/anie.202017031.

cial adsorbents, ion-exchangers, or catalysts. [2] As solid acid catalyst, their catalytic properties are not only determined by the acid properties or micropore size and geometry, but also by the morphology-dependent diffusion properties. ZSM-5 (MFI, zeolite framework code according to the International Zeolite Association) is among the most widely used zeolites in industrial applications, in processes such as propeneselective catalytic cracking, methanol-to-hydrocarbon (MTH) conversion, alkylation of aromatics, isomerization, etc. MFI contains sinusoidal 10-member ring (10-MR, 5.1 × 5.5 Å) channels along the a-axis, interconnected by straight 10-MR channels $(5.3 \times 5.6 \text{ Å})$ along the **b**-axis.^[3] Miniaturization of ZSM-5 crystals down to nanometer scale and generation of hierarchically porous structure have been found to be effective to enhance the transport property, acid site accessibility and catalytic performances.^[4] Especially, as molecules diffuse more rapidly along the straight channels than within the sinusoidal channels, [5] for the large pore dimension and low tortuosity, decrease of zeolitic domain size preferentially along b-axis is more influential to boost transport and catalytic properties. For instances, significant enhancement of catalyst lifetime and selectivity in methanol-togasoline (MTG)^[6] and methanol-to-olefin (MTO)^[7] conversions have been demonstrated when b-axis was reduced to a single unit cell thickness.

Towards this goal, decreasing the b-axis length of MFI crystals to less than 100 nm have been pursued by using designed SDAs such as bi-functional SDA that has a head group with hydrophilic diquaternary ammonium cations, [6] diquaternary ammonium cations, [8] tetrabutylphosphonium (TBPOH) induced repetitive branching (producing intergrown MFI/MEL house-of-cards), [9] multi-quaternary ammonium, [10] by taking advantage of the mismatch of these SDAs with the **MFI** framework that impedes crystal growth along baxis. However, these methods are dependent on the use of designed, unconventional SDAs that are economically prohibitive for practical use. It is also noteworthy that the preparation of unit cell thickness zeolite often interrupts the inherent crystalline structure of zeolites, and compromises their (hydro)thermal stability and acidity. The obtained zeolites are often Na+-form, which entails an ion-exchange process to afford the proton form, hence, producing voluminous waste water. On the other hand, fabrication of hierarchical zeolite by solely control of crystallization process in the absence of porogens often lead to the formation of MFI crystals with non-mesoporous core and an epitaxially grown, hierarchically structured shell.[11] The anisotropic growth of

13959







hierarchical ZSM-5 crystal with simple, commonly used starting materials through regulation of nucleation and crystal growth remains elusive, in particular, for the generation of **MFI** crystals with shortened **b**-axis thickness.

Herein, we report a Na⁺-free crystallization of hierarchical MFI crystals, comprising of b-axis reduced domains throughout the entire architecture, in the presence of commonly available tetrapropylammonium hydroxide (TPAOH) and tetrabutylammonium hydroxide (TBAOH) through homogeneous nucleation and a following-up SDA exchange induced reconstruction pathway. Such a synthesis avoids the use of expensive porogens and the ion-exchange process. Mesopores between zeolite domains has been constructed in a single crystallization step.

Results and Discussion

MFI zeolite often crystallizes as micrometer-sized crystals when using solely tetrapropylammonium cation (TPA⁺) as SDA, while tetrabutylammonium cation (TBA⁺) alone often leads to the formation of bulky ZSM-11 (MEL). Theoretical calculations implied that accommodation of all 4 intersections in one **MFI** unit cell only by 4 TBA⁺ molecules would give rise to space overcrowding and was therefore disfavored.[12] Previous co-templating synthesis using both TPA⁺ and TBA⁺ (and also Na⁺) only produces bulky, densely packed intergrown MFI/MEL crystals.^[13] It is postulated that TBA⁺, behaves like that of TBPOH, [9] is not well accommodated inside **MFI** channel intersections as that of TPA⁺. Therefore, a precise control of morphology could be achieved by tailoring nucleation and growth conditions in the co-presence of both SDAs.

The influence of TPA⁺/TBA⁺ ratio was first inspected for samples with Si/Al ratios of 50 and 100, respectively, with the reaction composition of 100 SiO_2 :0.5 (or 1.0) Al_2O_3 :(36-x) TBAOH:xTPAOH:400EtOH:1140H $_2$ O (x = 0, 0.5, 1, 2, 3, 4and 6). The corresponding X-ray diffraction (XRD) analyses (Figure S1, Supporting Information, SI) showed that the **MFI** phase could only be obtained when TPA+/TBA+ ratio was above 2:34, and below this value MEL was synthesized instead. The corresponding SEM images and N₂ physisorption data (Figure S2, S3 and Table S1, SI) demonstrated that the sizes of these agglomerates decreased with reducing TPAOH content and the sample derived from a TPA+/TBA+ ratio of 2:34 was found to possess the smallest crystal size and highest surface area. In regard of TPA⁺ occluded as-synthesized **MFI**, $|\left((C_3H_7)_4\text{-NOH}\right)_4|\left[Si_{96-x}Al_xO_{192}\right]$, this ratio ensures that both SDAs participate crystallization despite that TPA⁺ is preferred over TBA⁺ for the stronger interaction with inorganic framework. [14] The crystallization temperature was found suitable at 423 K to ensure proper crystallization time and high crystallinity (Figure S4, S5, SI). On the other hand, presence of Na⁺ should be avoided as Na⁺ could compete with other SDAs and is detrimental to the formation of hierarchical architecture^[6] (Figure S6, SI). In addition, extensive trials further demonstrated that monomeric silica (i.e., tetraethylorthosilicate, TEOS or tetramethylorthosilicate, TMOS) and Al (i.e., Al(i-PrO)₃, AlCl₃, Al₂(SO₄)₃) precursors were required, implying that homogeneous nucleation from clear suspension was indispensable for the formation of hierarchical structure (Figure S7, S8, SI). After narrowing down the above synthetic parameters, a series of ZSM-5-CT-x samples (x stands for the Si/Al ratio in the starting materials, x = 35– 200) were generated.

MFI phase for these samples was validated by collected XRD patterns (Figure S9a, SI). No product was recovered with Si/Al ratio of 25, possibly because of mismatch between low charge density, bulky SDAs and high charge density, low Si/Al ratio inorganic components.^[15] At higher Si/Al ratio of 150 and 200, the recipe would afford bulky crystals with smooth surfaces and insignificant amount of mesopores (Figure S9g-j, SI). The formation of large crystal may result from inconspicuous inhibiting effect of TBA+ over crystal growth at high Si/Al ratios. As the inorganic framework becomes less negatively charged as a result of increased Si/Al ratio, weakened attraction of TBA+ by growing crystal surface can be anticipated. Collectively, a typical crystallization of hierarchical MFI crystals was found to be feasible between Si/ Al ratio of 35 and 120.

The physicochemical properties of three representative samples, i.e., ZSM-5-CT-35, ZSM-5-CT-50 and ZSM-5-CT-100 were characterized, and comparisons were made with three control samples denoted as ZSM-5-C-x (with C standing for conventional synthesis and x representing Si/Al ratio in the starting materials, i.e., x = 35, 50, 100). XRD pattern (Figure S10, SI) revealed that pure phase MFI zeolite was obtained, while scanning electron microscopy (SEM) images revealed their typical coffin-like shape (Figure S11, SI). Elemental analyses showed that the Si/Al ratio of final products were slightly lower than that of staring materials (Table 1). The panoramic SEM image (Figure 1a) revealed that ZSM-5-CT-35 comprised of uniform particles with size ranges from 200 to 470 nm (average ca. 330 nm) in diameter. The enlarged SEM image shows that each particle consists of small plate-like primary units with a house-of-cards morphology. From the selected area electron diffraction (SAED) pattern, the four-fold symmetry can be observed, indicating the overlap of the a^* and b^* axes of the MFI structure from the common c axis with a 90° rotational epitaxial relationship (Figure 1b). The transmission electron microscopy (TEM) and high-resolution TEM (HRTEM) images also indicate the house-of-cards structure. The SAED pattern and TEM image taken from the common a/b axis of one particle are shown in Figure S12, SI. The HRTEM image and the corresponding Fourier diffractogram (FD) perpendicular to the primary plate show the typical contrast and the characteristic diffraction pattern of the **b** axis of **MFI** crystals. Therefore, each primary plate is grown along the a-c plane and the thickness of the **b**-axis is greatly reduced to several pentasil layers (5– 14 nm), as indicated in the schematic representation (Figure 1e). This arrangement generates abundant amount of mesoporosity, similar to the report by Tsapatsis et al. [9] The overlapping feature of the small nanosheets makes it difficult to determine the detailed connectivity if the MEL structure is

On the other hand, the average particle diameter of ZSM-5-CT-50 was increased to ca. 420 nm. The enlarged SEM



Research Articles



Table 1: Si/Al ratio, textural, diffusion properties and acidity of ZSM-5 samples derived from the results of elemental analysis, Ar physisorption results, diffusivity measurements of 2,2-dimethylbutane and Py-IR measurements.

Sample	Si/Al ^[a]	S_{BET} $[m^2g^{-1}]^{[b]}$	$S_{ext} = [m^2 g^{-1}]^{[c]}$	V_{micro} ([cm ³ g ⁻¹] ^[c]	$V_{\rm meso}$ [cm 3 g $^{-1}$] ^[d]	Brønsted acid density $[\mu mol g^{-1}]^{[e]}$	Lewis acid density $[\mu mol g^{-1}]^{[e]}$	$D_{\rm eff}/R^{2[f]}$	TON ^[g]
ZSM-5-C-35	33	292	35	0.11	0.11	233	54	3.47×10^{-6}	1.21×10^{3}
ZSM-5-CT-35	34	426	164	0.11	0.48	121	200	1.67×10^{-4}	6.45×10^{3}
ZSM-5-C-50	46	323	45	0.08	0.12	206	35	2.84×10^{-6}	1.92×10^{3}
ZSM-5-CT-50	42	532	293	0.09	0.64	218	107	9.89×10^{-5}	1.13×10^{4}
ZSM-5-C-100	83	352	61	0.13	0.10	126	19	3.00×10^{-6}	4.32×10^{3}
ZSM-5-CT-100	83	451	280	0.12	0.40	132	50	7.47×10^{-6}	4.48×10^4

[a] Determined by inductively coupled plasma atomic emission spectrometry (ICP-AES). [b] Calculated by the Brunauer–Emmett–Teller (BET) method. [c] Deduced by the *t*-plot method. [d] Calculated from Barret–Joyner–Halenda (BJH) method. [e] Calculated corresponding to Py-IR spectra desorbed at 573 K; [f] Calculated by the diffusivity measurements corresponding to Figure 5 a. [g] The turnover number (TON) considered as the accumulated number of dimethyl ether (DME) molecules converted per Al site.

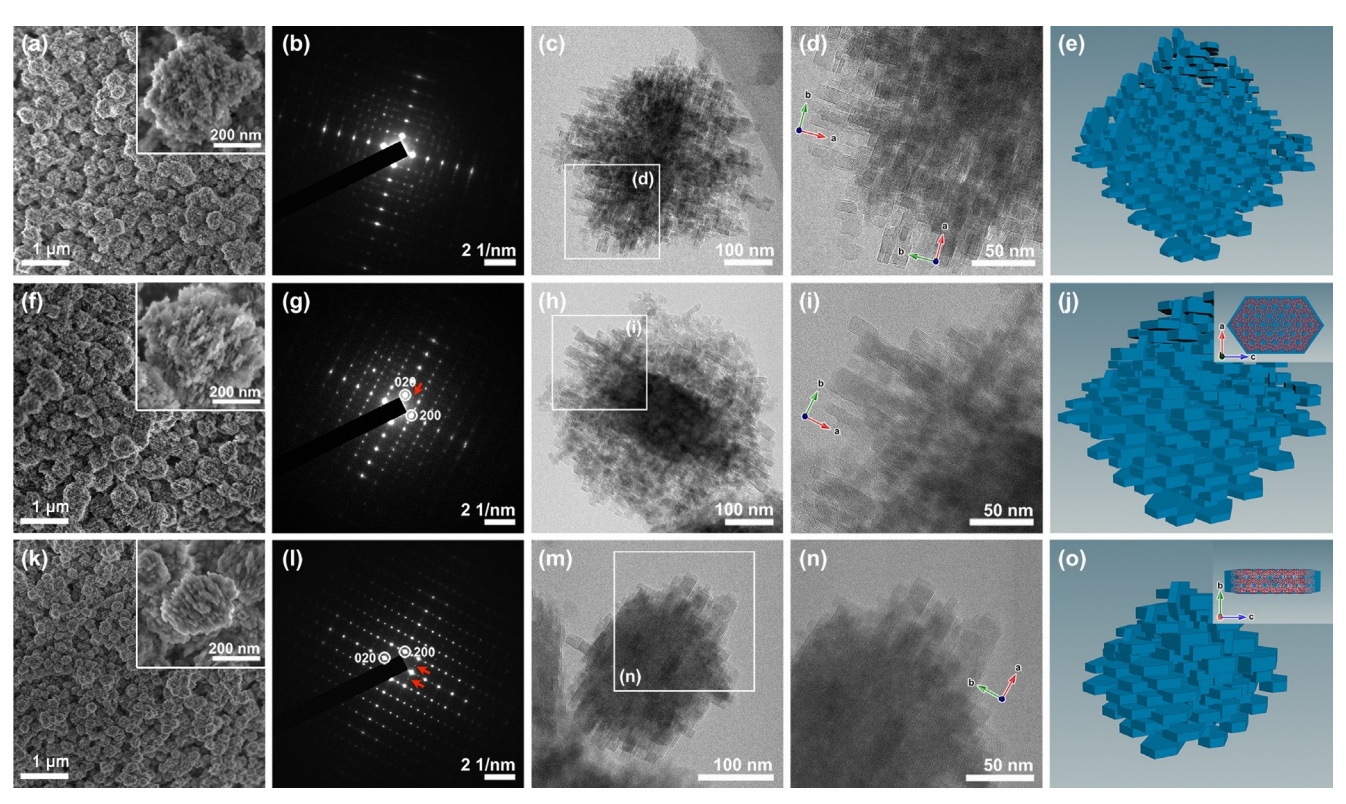


Figure 1. FE-SEM, TEM images, the corresponding SAED patterns and representations for ZSM-5-CT-35 (a–e), ZSM-5-CT-50 (f–j) and ZSM-5-CT-100 (k–o).

image shows that the particle is formed by the ordered stacking of plate- like primary units (Figure 1 f), recommending a non-classic oriented attachment growth history. The alignment of primary crystallites is also evidenced in SAED and the corresponding TEM images (Figure 1 g-i). The SAED pattern taken from the c axis of ZSM-5-CT-50 shows the typical single crystal feature with nice crystallinity, indicating each particle is basically a single crystal composed of primary MFI plates. Each primary MFI plate is grown along the a-c plane and the b-axis is increased to 8–23 nm. Extra spots with very weak diffraction intensity can be also observed, as indicated by red arrows in the SAED pattern, are corresponding to the same MFI structure with 90° rotational relationship along the common c axis, suggesting a small number of plates are perpendicularly intergrown in the

particle, which could contribute to the formation of domain boundaries.^[17] The structural feature is further confirmed in HRTEM image (Figure 1i). A large amount of interlayer space (meso- and macro- porosity) has been created in this sample due to the hierarchical structure. ZSM-5-CT-100 shows a similar structural feature (Figure 1 k-o), except that the diameter of the individual particle generally reduced to ca. 210 nm and the size of the primary plates were generally increased. The single crystalline feature is also observed for this sample. It is worthy to note that the sample ZSM-5-CT-100 has the highest orientational order of the primary units. The schematic model is displayed in Figure 1 o, to illustrate the architecture.

Three-dimensional (3D) electron tomographic reconstruction of ZSM-5-CT-x (Figure 2 and Videos S1–S6, SI)







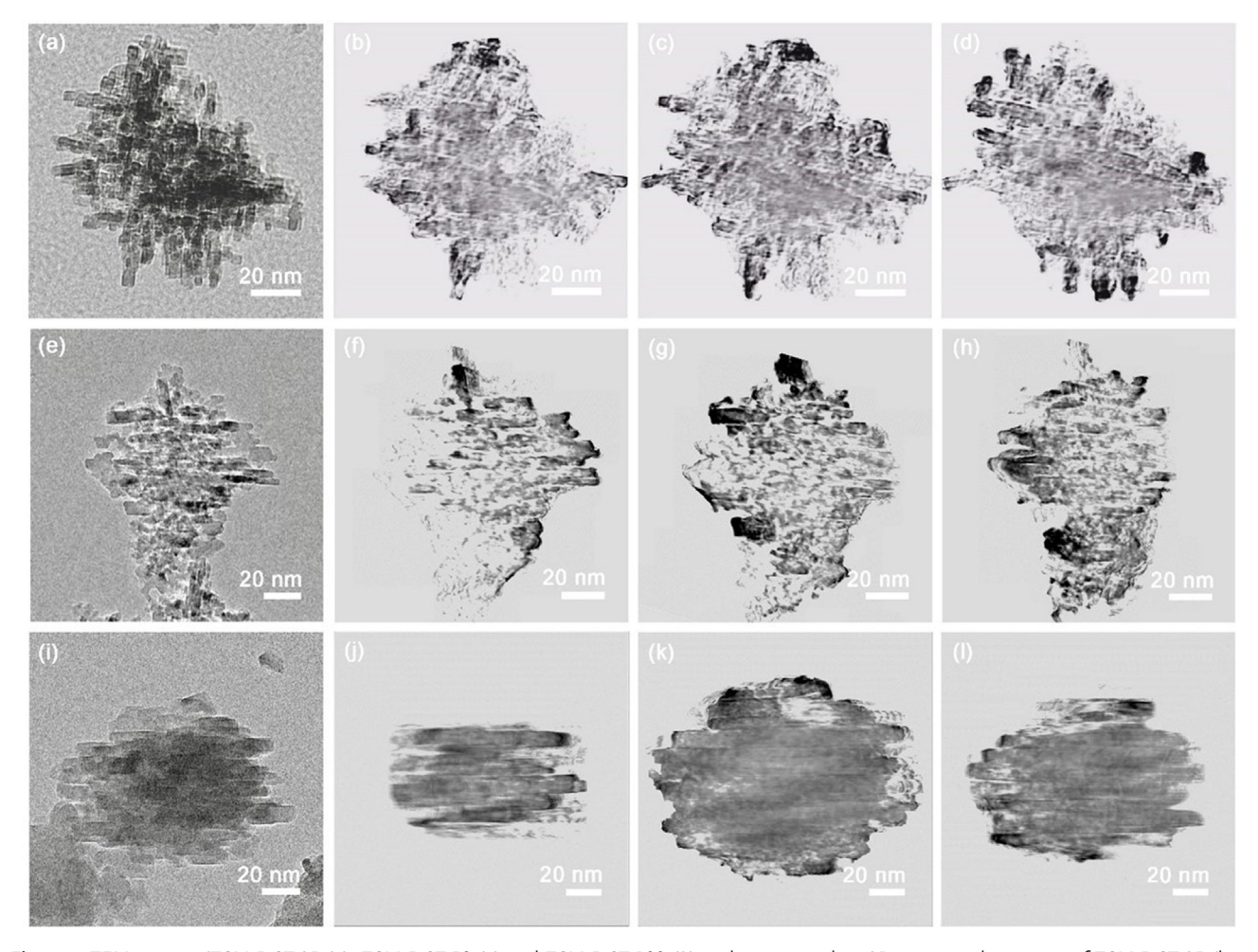


Figure 2. TEM images (ZSM-5-CT-35 (a), ZSM-5-CT-50 (e) and ZSM-5-CT-100 (j)) and corresponding 3D tomography images of ZSM-5-CT-35 (b–d), ZSM-5-CT-50 (f–h) and ZSM-5-CT-100 (j–l) crystals showing cross-sectional snapshots from Videos S1, S3 and S5, S1, respectively.

further confirmed that the interior of particle is constructed by **b**-axis shortened **MFI** primary units, which is different from hierarchical structures reported recently.^[11] TEM tomograms of ZSM-5-CT-*x* (Figure 2b-d, f-h and j-l for ZSM-5-CT-35, ZSM-5-CT-50 and ZSM-5-CT-100, respectively, at the location from top to bottom near the center of the particles) clearly show that the internal structure of the stacking domains is consistent with that of the external ones. Between crystalline domains, porous regions could be clearly visualized.

Notably, the reduction of **MFI** crystal thickness for these sample implies a significant enhancement of transport properties with respect to other shapes. Overall, **b**-axis reduced hierarchical **MFI** crystals have been generated within Si/Al of 35 to 120, and the lower the Si/Al ratio, the more uniform the structure becomes.

The textural properties were measured by Ar physisorption isotherms, and the inferred data were outlined in Table 1 and Figure S13, SI. The control samples, ZSM-5-C-35, ZSM-5-C-50 and ZSM-5-C-100, exhibited a steep uptake curve at relative pressure $P/P_0 < 10^{-3}$ ascribed to micropore filling. In ZSM-5-CT-35, ZSM-5-CT-50 and ZSM-5-CT-100, jump of Ar uptakes at $P/P_0 > 0.80$ was also observed, owing to capillary

condensation inside the secondary meso- or macro- pores between interlayer space formed by the stacking of primary plates. Complementary mercury intrusion measurements were also employed to estimate porosity. The deduced data were displayed in Figure S14, SI. The distributions of poresize verified the presence of 62, 40 and 40 nm macro-/mesopores on ZSM-5-CT-35, ZSM-5-CT-50 and ZSM-CT-100, respectively. It is noteworthy that mercury intrusion measures penetrating meso- and macro- pores that are accessible through external surface that are beneficial to transport properties.^[18] The measured BET surface areas are 426, 532 and 451 m² g⁻¹, for ZSM-5-CT-35, ZSM-5-CT-50 and ZSM-5-CT-100, respectively, which are larger with respect to their microporous counterparts (292, 323 and 352 m² g⁻¹ for ZSM-5-C-35, ZSM-5-C-50 and ZSM-5-C-100, respectively). The increase in surface area, in line with SEM and TEM observations, arising from increased external surface area and decrease of crystal size (Table 1). Micropore volumes were nearly unchanged, verifying that the intrinsic microporosity of MFI crystal structure was largely preserved, which agreed with XRD results.

²⁷Al MAS NMR spectra for calcined samples (Figure S15a, SI) showed one major resonance peak sitting at





ca. 56 ppm and negligible quantities ca. -2.0 and 1.0 ppm associated with extra- framework, octahedrally coordinated Al moieties, manifesting that most Al was incorporated as tetrahedral AlO₄⁻ into the framework of MFI. ²⁹Si MAS NMR spectra (Figure S15b, SI) could be deconvoluted into four peaks centered at ca. -116, -113, -107, and -103 ppm, respectively. ZSM-5-CT-35 (70.5% and 17.9%), ZSM-5-CT-50 (67.8% and 14.0%) and ZSM-5-CT-100 (63.9% and 22.0%) exhibited a major broad signal at approximately -113 and -116 ppm, which could be attributed to $Q^4 = [Si-$ (OSi)₄],^[19] suggesting that they were less condensed compared with control samples except for ZSM-5-CT-35 (ZSM-5-C-35: 85.8% and 2.6%; ZSM-5-C-50: 75.6% and 14.9%; ZSM-5-C-100: 84.8% and 8.9%, Table S2 and Table S3, SI). The heterogeneous broadening was ascribed to Si locating on the 12 T-sites. [20] Besides, the small resonance peak centered at ca. -103 and -107 ppm could be distinguished in ZSM-5-CT-35 (0.3 and 11.3%), ZSM-5-CT-50 (8.5 and 9.7%) and ZSM-5-CT-100 (9.4 and 4.7%). The peak is assigned here to the contribution from surface $Q^3 = [Si(OSi)_3(OH)]$ and framework [Si(OSi)₃(OAl)] moieties, respectively, by referring to ²⁷Al MAS NMR data, ²⁹Si CP/MAS NMR (Figure S16, SI) and reported ones.[21] Hence, the NMR data evidenced that the short range order in the obtained materials was comparable to that in the control samples except the presence of large external surface areas and mesopore volumes.

Since the hierarchical architecture was formed during the crystallization in the absence of porogens, it is important to understand the formation mechanism and controlling synthesis parameters. To this end, the crystallization processes of ZSM-5-CT-50 and ZSM-5-CT-100 were monitored using combined ex situ XRD, SEM, TEM and MAS NMR characterizations. It was assumed that quenching of crystallization would freeze structure evolution in hydrothermal synthesis. No solid product could be recovered from the

growth solution before 6 h for ZSM-5-CT-50. Time-dependent XRD patterns and the corresponding crystallization curve of ZSM-5-CT-50 (Figure 3 a,b) showed, abnormally, that the 8 h collected sample possessed a high relative crystallinity (RC, calculated by integrating the peak areas at 2θ range from 7° to 9°, 22.5° to 25° and referred to the final product, presetting as 100%) of 89.1%, [22] which declined to 61.2% at 9 h before growing again with prolonged time. The temporal evolution of morphology recorded by SEM (Figure S17, SI) and TEM images (Figure 3c-h) demonstrated that the 6 h sample was made of uniform, loosely packed particulates of ca. 170 nm with rough surfaces. SEM tracking disclosed that surface roughening corresponding to the primary plates started from 8 h on, and became clearly visible at 9 h, accompanied by a distinct increase of mean particle size to 300 nm. Thereafter, crystals gradually grew from 300 nm to 400 nm and porous regions were developed in a recrystallization process. The corresponding temporal TEM images (Figure 3c-h) demonstrated that recrystallization started from 8 h on, the thickness contrast indicating the formation of primary plates (inset of Figure 3d), and further growth was escorted by core area dissolution. From 24 h on, the growth of primary crystalline plates in the marginal regions was identified, associated with the further crystallization process. No morphological characteristics of early particles could be observed, indicating recrystallization extended into the interior parts of crystals.

Solid state MAS NMR spectra for the crystallization series were recorded to monitor the changes in both occluded SDAs and framework elements, to gain molecular level understanding of formation process. ¹³C MAS NMR spectra (Figure 4) manifested that TBA⁺ was found to be the mainly occluded SDA in the separated gel (collected via rotary evaporation at 353 K) in the early stage of nucleation (5 h), as shown by the chemical shifts at 60.9, 24.4, 20.3 and 14.4/

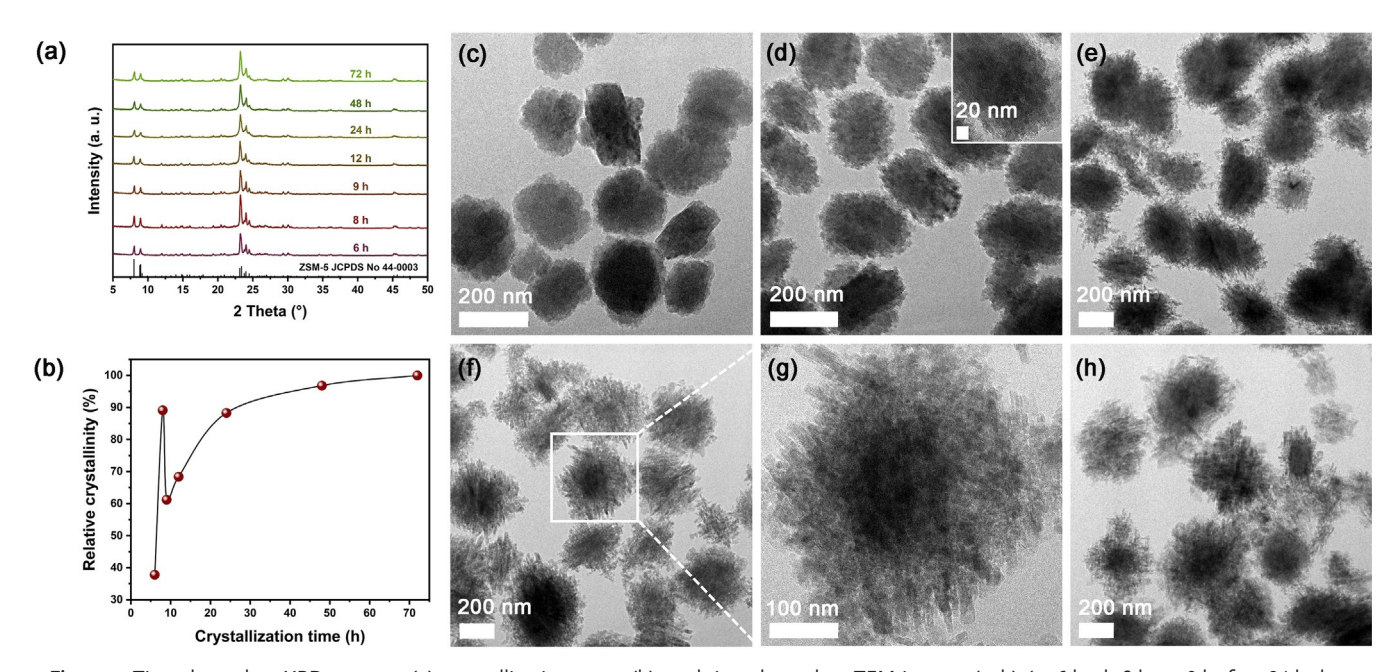
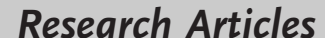


Figure 3. Time-dependent XRD patterns (a), crystallization curve (b), and time-dependent TEM images (c-h) (c: 6 h; d: 8 h; e: 9 h; f-g: 24 h; h: 48 h) for ZSM-5-CT-50 during crystallization.







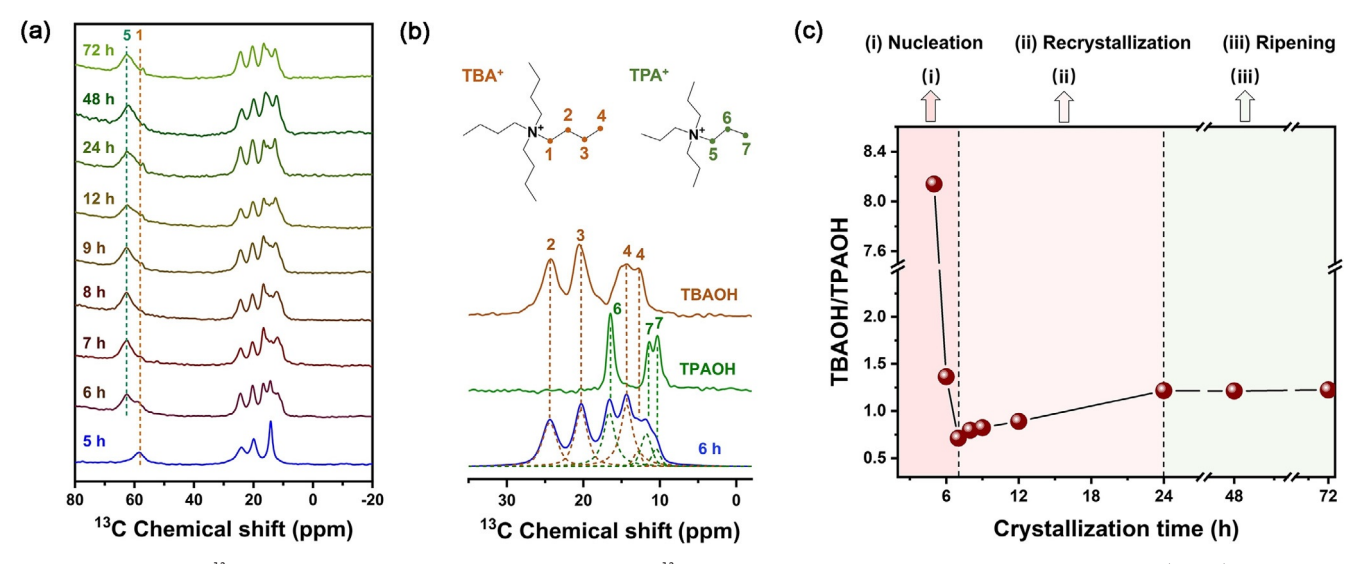


Figure 4. Solid-state ¹³C MAS NMR spectra (a), peak fitting method of ¹³C MAS NMR spectra (b), and the change curve of TBA⁺/TPA⁺ ratio (c) for as-synthesized ZSM-5-CT-50 in the course of crystallization. The relative value of TBA⁺/TPA⁺ was calculated by using the formula $((S_2 + S_3 + S_4)/3)/((S_6 + S_7)/2)$, where S_n represents the peak area of the corresponding peak of n, n represents the number noted in (b).

12.8 ppm, which originated from C1, C2, C3 and C4 in the TBA⁺. A small amount of TPA⁺ could also be detected, indicating resonance peaks at 63.2, 16.5 and 11.4/10.4 ppm, associated with C5, C6 and C7 in the molecule. Split of resonance peaks can be explained by the position of SDA locating at the micropore intersection between straight and sinusoidal positions. [19] The broadening of resonance peaks for SDAs could be caused by the co-presence of encapsulated and surface adsorbed SDAs in TPA-TEOS crystallization system.[23] Deconvolution and quantification of TBA+/TPA+ ratio change with crystallization time was plotted in Figure 4c, indicating a high ratio of 8.1 before condensation at 5 h. The TBA+/TPA+ ratio at 6 h dropped to 1.4 when crystalline structure of MFI could be observed, and a minimum of 0.7 was detected at 7 h, which progressively increased to 1.2 at 24 h and maintained constant afterwards. Considering the nominal TBA+/TPA+ ratio of 17 in the growth solution, obviously, a preferential encapsulation of TPA⁺ over TBA⁺ during both nucleation and recrystallization processes was observed, as the former could better stabilize MFI framework. [14] 27Al MAS NMR spectra (Figure S18a, SI) displayed one resonance signal at 56.2 ppm assignable to tetrahedral AlO₄ units in amorphous silica matrix at 5 h, which, gradually shifted towards 54 ppm, coinciding with SDA exchange and recrystallization process, hence, suggesting a stronger SDA-framework interaction for TPA⁺ than that of TBA⁺. The concurrent ²⁹Si MAS NMR spectrum (Figure S18b, Table S4 and Table S5, SI) of 5 h sample before condensation contained three broad, partially overlapping resonance signals at -88.4 (11.6%), -98.3 (56.8%), and -109.1 (12.0%) ppm, associated with amorphous Q^2 , Q^3 and Q4 29Si in polysilicate units, respectively. [21b,24] The high contents of Q² and Q³ in 5 h sample indicated poor degree of long-range order and less cross-linking at early stage of nucleation, i.e., the sample consisted mainly of partially condensed oligomers of silica together with incorporated Al in tetrahedral coordination. At 6 h, when solid powder could be collected, the resonance intensity of peaks corresponding to amorphous species decreased considerably to insignificant amounts (2.9% in normalized integral area). Meanwhile, ²⁹Si signals associating with Q^3 (-101.0 ppm) and Q^4 (-112.7 ppm, -116.1 ppm) moieties in crystalline phase increased rapidly to 16.4% and 67.2%, suggesting a quick homogeneous nucleation from clear solution. [24] Subsequently, the amorphous phase decreased gradually and was completely consumed, as only the ones of crystalline MFI phase could be detectable. With the evolution of order, the chemical shift for Q4 remained virtually the same, while the signal for Q^3 moieties shifted from -101 to -103 ppm from 9 h till the end of crystallization. As the shift was escorted by TPA⁺/TBA⁺ exchange, which could be tentatively ascribed to a stronger Coulomb attraction of negatively charged [Si-(OSi)₃(OAl)] moieties by neighboring, charge balancing TPA⁺. This assignment is reasonable, since [Si(OSi)₃(OH)] contribution to O³ tends to decrease with degree of condensation and prolonged crystallization time. The overall Q³/ Q⁴ ratio versus crystallization time variations were plotted in Figure S18c, SI. The maximum percentage of Q³ moieties appears in recrystallization (8 h), then reached the lowest in the final crystallization sample. The crystallization tracking for the formation of ZSM-CT-100 (Figure S19–S21, SI), likewise, conformed to the same rule. Conversely, the formation of ZSM-5-C-50 (Figure S22, SI) or ZSM-5-C-100 (Figure S23, SI) was found to follow another route. Together, by correlating with aforementioned characterizations, SDA exchange induced recrystallization (SEIR) is responsible for the formation of such architectures.

The yields of solids, their respective Si/Al ratios and SDA contents were also tracked, as outlined in Figure S24, SI. The solid yields for both ZSM-5-CT-50 and ZSM-5-CT-100 were found to increase with prolonged hydrothermal heating time. Meanwhile, a continuous decrease of Si/Al ratio from ca. 140 to approximately the final products composition was observed. The early time yields (6–9 h) were low because it was

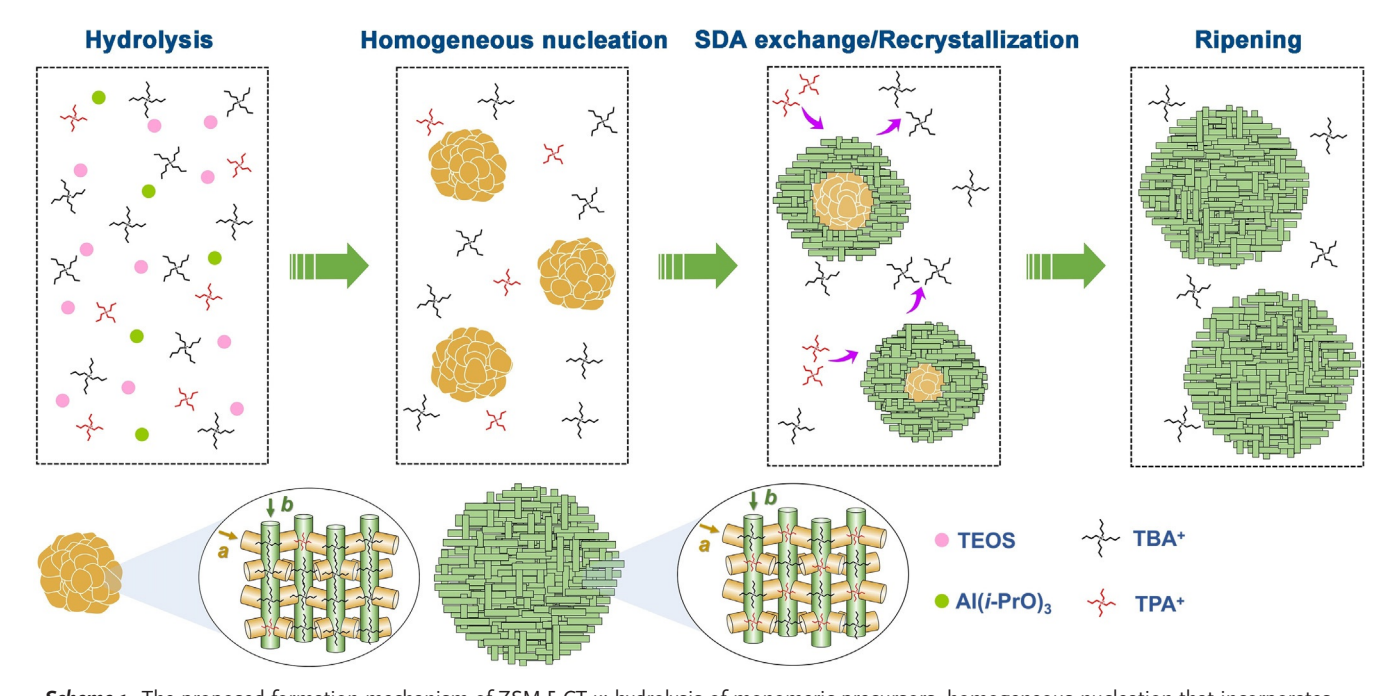




only the nuclei that were collected. It is no surprise that solid yield would increase thereafter as these nuclei exerted a seeding effect and dissolution of nuclei and recrystallization occurred simultaneously. The Si/Al ratios of solids in the early heating time were much higher than that of the initial gel, indicating a preferential formation of high Si/Al ratio nuclei. Both the Si/Al ratio and solid yield became flattened at a value close to compositions of products after 24 h of hydrothermal treating. By correlating TBA⁺ to TPA⁺ content variations with the concomitant changes of Si/Al ratio, one may find that the initial gel has a higher Si/Al ratio because the nucleation is driven by a mixture with high TBA⁺ and low TPA⁺ content, and the low charge density of TBA⁺ favors high Si/Al ratio of framework. Along with recrystallization process, the Si/Al ratio of the framework decreases as more TPA⁺ replaces TBA⁺ and the overall content of encapsulated SDAs remains virtually constant.

On the ground of the above experiments, and also referring to crystallization in TPA-TEOS clear solution, [24,25] a putative crystallization mechanism can be proposed as sketched in Scheme 1 for ZSM-5-CT-x. In the early stage, monomeric inorganic precursors hydrolyze and encapsulate both TBA+ and TPA+ to produce amorphous, embryonic zeolite suspensions (apparent clear solution), which quickly condenses into loosely packed, semi-crystalline particulates. Since nucleation is driven mainly by TBA⁺ (because of insufficient TPA⁺ in the gel), and also as a requirement of charge balance, more TBA+ has been encapsulated in the nucleated high Si/Al ratio particulates. Since TBA+-MFI interaction is relatively weak with respect to TPA+-MFI system, [12] the loosely packed and less ordered particulates tend to dissolve and recrystallize, induced by TPA+ substitution of TBA⁺. As the amount of available TPA⁺ in the mother liquor could not fulfill all the intersections in MFI lattice. TBA⁺ therefore also serves as co-SDA in this recrystallization process. With the progress of recrystallization and ripening, the predominant surface adsorbed species becomes TBA⁺ as the majority of TPA⁺ has been consumed and incorporated into the crystal lattices. TBA+ has a better fit to the pore openings of straight channels along b-axis, and the decoration of crystal surface by TBA⁺ could suppress the crystal growth along **b**-axis by stabilizing the **a-c** plane. [24,25] Since external surface adsorption of SDAs originates from either strong AlO₄⁻-TBA⁺ or weak surface -SiO⁻-TBA⁺ pairs, and the respective contribution is dependent on framework Si/Al ratios. At low Si/Al ratios, the former could contribute more to a stronger inhibition effect and the plate-like morphology is well developed. This also explains why the synthesis of hierarchical structure failed in the presence of Na⁺ or at very high Si/Al ratios (i.e., 150). Crystalline, hierarchical structure is evolved during the ripening process.

Before catalytic tests, the acid and diffusion properties were measured by standard pyridine adsorbed Infrared spectroscopy (Py-IR) and gravimetric method, respectively. The results are compiled in Table 1, Table S6, Figure S25, SI and Figure 5. ZSM-5-CT-35 (121 μmol g⁻¹) showed decreased medium-to-strong Brønsted acid site density (measured at 573 K) with respect to ZSM-5-C-35 (233 μmol g⁻¹), while the values for ZSM-5-CT-50 (218 μmol g⁻¹) and ZSM-5-C-50 (206 μmol g⁻¹), ZSM-5-CT-100 (132 μmol g⁻¹) and ZSM-5-C-100 (126 μmol g⁻¹) were comparable. More Lewis sites and less Brønsted sites were measured on ZSM-5-CT-35 with respect to their conventional counterparts. Formation of Lewis acid site out of dihydroxylation and dealumination of Brønsted acid site sitting at the external surface is likely the reason, ^[26] and increment of external surface area often



Scheme 1. The proposed formation mechanism of ZSM-5-CT-*x*: hydrolysis of monomeric precursors, homogeneous nucleation that incorporates both SDAs and produces semi-crystalline particulates, SDA exchange induced dissolution-recrystallization and hierarchical order development in ripening process.





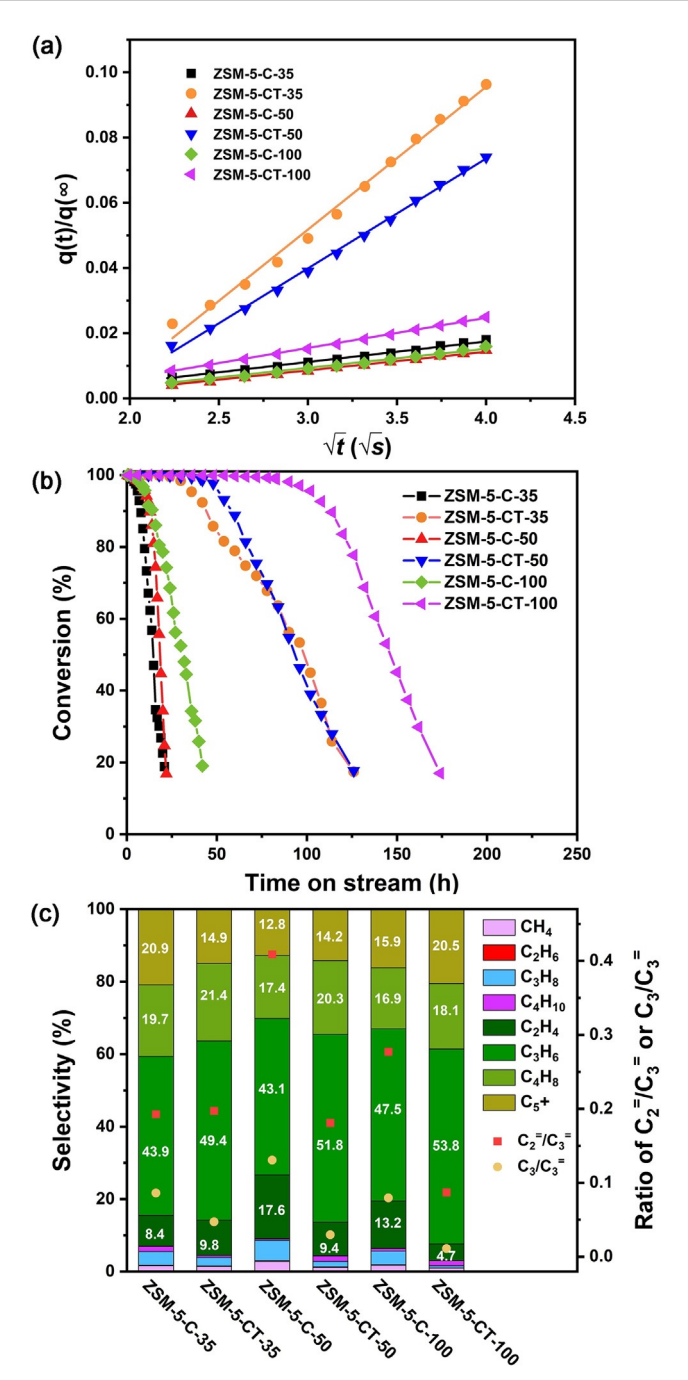


Figure 5. Adsorption rates of 2,2-dimethylbutane in the calcined ZSM-5 zeolites (a), DME conversion with TOS (b) and overall product slates (c) when the DME conversion exceeds 95% in the reaction system of DTO on various ZSM-5 samples. Reaction temperature: catalyst loading, 0.10 g, 723 K, WHSV = $4 h^{-1} g_{-DME} g_{-cat}^{-1}$.

induces formation of more Lewis acid sites in hierarchical zeolites. [27] 2,2-dimethylbutane was used as probe molecule in the gravimetric measurements for its kinetic diameter (6.3 Å) is close to micropore dimension of **MFI** structure. [28] The diffusion properties were obtained quantitatively by Fick's second law. The initial adsorption was often used to calculate diffusivity because it was not sensitive to the heat of adsorption. [28] $q(t)/q(\infty)$ showed a good linear relationship with \sqrt{t} as shown in Figure 5 a. The values of $D_{\rm eff}/R^2$ (Table 1)

deduced from the slope of the adsorption profiles have increased 48.1, 34.8 and 2.5 times for ZSM-5-CT-35, ZSM-5-CT-50 and ZSM-5-CT-100, respectively, with respect to control samples. The increase of $D_{\rm eff}/R^2$ represents the shortening of effective diffusion lengths (R) as a consequence of the reduction of b-axis thickness. The diffusion property improvements coincide with TEM observations of structure, i.e., more uniform samples with low Si/Al ratio exhibit better transport performance.

The catalytic properties for ZSM-5-CT-35, ZSM-5-CT-50 and ZSM-5-CT-100 were evaluated in catalytic conversion of dimethyl ether-to-olefin (DTO), and were compared with the microporous control samples. The DTO reaction was carried out on an atmospheric fixed-bed reactor at 723 K with a space velocity of 4 h⁻¹ g_{-DME} g_{-cat}⁻¹. The conversion versus time-onstream were depicted in Figure 5b, prolonged catalyst lifetime, for ZSM-5-CT-35 (36 h), ZSM-5-CT-50 (51 h) and ZSM-5-CT-100 (103 h) with respect to ZSM-5-C-35 (6 h), ZSM-5-C-50 (8 h) and ZSM-5-C-100 (10 h), were observed, respectively. Polyaromatic compounds derived from aromatic intermediates are the cause of catalyst deactivation. The expansion in catalyst lifetime reflects that less aromatics were formed from hydride transfer reaction on hierarchical catalysts, which is more prominent at low acid site density.^[29] The deduced turnover numbers (TONs), defined as the accumulated number of dimethyl ether (DME) molecules converted per Al site, of ZSM-5 samples are shown in Table 1, which can be used to accurately evaluate their catalytic activity. [30] The TONs of ZSM-5-CT-x (x = 35, 50 and 100 respectively) are 5.33, 5.88 and 10.37 times that of the control samples, which agrees well with their enhanced diffusion properties. The corresponding integral product slates for light hydrocarbons were shown in histograms in Figure 5c. Within the product slates, more light olefins (mainly, ethene and propene), in particular, propene was produced by the hierarchical catalysts, ZSM-5-CT-35 (49.4 % vs. 43.9 %), ZSM-5-CT-50 (51.8 % vs. 43.1%) and ZSM-5-CT-100 (53.8% vs. 47.5%), with respect to the microporous counterparts. It is also observed that less ethene is produced in hierarchical samples with respect to the control samples, as reflected by ethene/propene ratio variations. From mechanistic knowledge, ethene is produced solely by aromatic- mediated cycle, while propene can be generated by both olefinic and aromatic cycles (with the former more efficient than that of the latter), [31] hence, the ratio variations, as a measure of cycle dominance, disclose that aromatic cycle-based conversion is disfavored by the shortening of retention time as a result of b- axis reduction.^[7] In addition, aromatic cycle dominates at high acid site density explains the impact of Si/Al ratios. [32] Propane is regarded as a hydride transfer product from propene, hence, the variations of propane/propene ratios among samples reflect the impact of hydride transfer over selectivity. The higher the ratio, the more olefins are transformed to paraffins. [33] Likewise, much lower fraction of paraffins, such as CH4 (as a product of hydride transfer from CH₃-Z), [34] is produced on ZSM-5-CT-x. Besides, $C_4^{=}$, which is considered as product or intermediate of olefin-based cycle, is shown to increase handin-hand with that of propene selectivity, lending a further







evidence for the exaggeration of olefinic cycle by the presence of hierarchical architecture.

Overall, high propene selectivity and resistance to coking, which are the two most important parameters in DTO catalysts, have been attained on *b*-axis reduced **MFI** crystal, as a consequence of suppression of the aromatic cycle stemming from enhanced transport property and attenuated Brønsted acid site density.^[32]

Conclusion

The co-presence of both TPAOH and TBAOH permitted the synthesis of self-assembled hierarchical MFI zeolite with reduced b-axis without using mesoporogens. Homogeneous nucleation from clear solution and the use of monomeric Al and Si sources have been identified as key factors influencing the structure of final products. The disclosed SDA exchange induced anisotropic recrystallization is found to be Si/Al ratio- dependent, hence, allowing tailoring of crystal morphology between Si/Al ratio between 35 and 120, and b-axis reduction down to tens of nanometers could be effectively achieved preferably at 35 to 100. Hierarchical MFI zeolite showed an increased propene selectivity and catalyst lifetime in DTO conversion, owing to the enhanced transport efficiency and suppressed side reactions. As many zeolites can be generated by more than one SDAs, and each SDA exerts distinct stabilization effect on the same framework, this synthetic strategy is expected to be extendable to the control of zeolite morphology. Moreover, the catalytic advantage resulting from reduced **b**-axis deserves future explorations.

Acknowledgements

K.Z., S.X., and L.H. are grateful for the financial support from National Natural Science Foundation of China (21878079, K.Z.; 21972142 and 22022202, S.X.; 21922304 and 21873072, L.H.). S.X. also acknowledge the funding from Liao Ning Revitalization Talents Program (XLYC1807227).

Conflict of interest

The authors declare no conflict of interest.

Keywords: dimethylether-to-olefin · hierarchical architecture · **MFI** zeolite · recrystallization · reduced **b**-axis thickness

- [1] C. S. Cundy, P. A. Cox, Chem. Rev. 2003, 103, 663-701.
- [2] M. E. Davis, *Nature* **2002**, *417*, 813 821.
- [3] D. H. Olson, G. T. Kokotailo, S. L. Lawton, W. M. Meier, J. Phys. Chem. 1981, 85, 2238–2243.
- [4] a) D. Kerstens, B. Smeyers, J. Van Waeyenberg, Q. Zhang, J. Yu, B. F. Sels, Adv. Mater. 2020, 32, 2004690; b) L. Chen, M. Sun, Z. Wang, W. Yang, Z. Xie, B. Su, Chem. Rev. 2020, 120, 11194–11294.
- [5] M. Baumgärtl, A. Jentys, J. A. Lercher, J. Phys. Chem. C 2019, 123, 8092–8100.

- [6] M. Choi, K. Na, J. Kim, Y. Sakamoto, O. Terasaki, R. Ryoo, Nature 2009, 461, 246-249.
- [7] R. Khare, A. Bhan, J. Catal. 2015, 329, 218-228.
- [8] S. H. Keoh, W. Chaikittisilp, K. Muraoka, R. R. Mukti, A. Shimojima, P. Kumar, M. Tsapatsis, T. Okubo, *Chem. Mater.* 2016, 28, 8997–9007.
- [9] X. Y. Zhang, D. X. Liu, D. D. Xu, S. Asahina, K. A. Cychosz, K. V. Agrawal, Y. Al Wahedi, A. Bhan, S. Al Hashimi, O. Terasaki, M. Thommes, M. Tsapatsis, *Science* 2012, 336, 1684– 1687.
- [10] a) D. Xu, Y. Ma, Z. Jing, L. Han, B. Singh, J. Feng, X. Shen, F. Cao, P. Oleynikov, H. Sun, O. Terasaki, S. Che, *Nat. Commun.* **2014**, *5*, 4262; b) A. Chang, H. M. Hsiao, T. Chen, M. Chu, C. Yang, *Chem. Commun.* **2016**, *52*, 11939–11942.
- [11] a) K. L. Ding, A. Corma, J. A. Macia-Agullo, J. G. Hu, S. Kramer, P. C. Stair, G. D. Stucky, J. Am. Chem. Soc. 2015, 137, 11238–11241; b) H. Dai, Y. Shen, T. Yang, C. Lee, D. Fu, A. Agarwal, T. T. Le, M. Tsapatsis, J. C. Palmer, B. M. Weckhuysen, P. J. Dauenhauer, X. Zou, J. D. Rimer, Nat. Mater. 2020, 19, 1074–1080.
- [12] E. de Vos Burchart, H. van Koningsveld, B. van de Graaf, Microporous Mater. 1997, 8, 215–222.
- [13] a) G. R. Millward, S. Ramdas, J. M. Thomas, M. T. Barlow, J. Chem. Soc. Faraday Trans. 2 1983, 79, 1075-1082; b) G. A. Jablonski, L. B. Sand, J. A. Gard, Zeolites 1986, 6, 396-402.
- [14] V. Shen, A. T. Bell, Microporous Mater. 1996, 7, 187-199.
- [15] G. J. Lewis, M. A. Miller, J. G. Moscoso, B. A. Wilson, L. M. Knight, S. T. Wilson, Stud. Surf. Sci. Catal. 2004, 154, 364–372.
- [16] M. K. Choudhary, M. Kumar, J. D. Rimer, Angew. Chem. Int. Ed. 2019, 58, 15712–15716; Angew. Chem. 2019, 131, 15859–15863.
- [17] L. Karwacki, M. H. F. Kox, D. A. M. de Winter, M. R. Drury, J. D. Meeldijk, E. Stavitski, W. Schmidt, M. Mertens, P. Cubillas, N. John, A. Chan, N. Kahn, S. R. Bare, M. Anderson, J. Kornatowski, B. M. Weckhuysen, *Nat. Mater.* 2009, 8, 959–965.
- [18] M. Milina, S. Mitchell, P. Crivelli, D. Cooke, J. Perez-Ramirez, Nat. Commun. 2014, 5, 3922.
- [19] P. Magusin, V. E. Zorin, A. Aerts, C. J. Y. Houssin, A. L. Yakovlev, C. E. A. Kirschhock, J. A. Martens, R. A. van Santen, J. Phys. Chem. B 2005, 109, 22767 22774.
- [20] C. A. Fyfe, H. Grondey, Y. Feng, G. T. Kokotailo, J. Am. Chem. Soc. 1990, 112, 8812–8820.
- [21] a) R. J. Messinger, K. Na, Y. Seo, R. Ryoo, B. F. Chmelka, Angew. Chem. Int. Ed. 2015, 54, 927–931; Angew. Chem. 2015, 127, 941–945; b) J. K. Reddy, K. Motokura, T. R. Koyama, A. Miyaji, T. Baba, J. Catal. 2012, 289, 53–61.
- [22] H. Chen, X. Shi, J. F. Liu, K. C. Jie, Z. H. Zhang, X. B. Hu, Y. M. Zhu, X. Y. Lu, J. Fu, H. Huang, S. Dai, J. Mater. Chem. A 2018, 6, 21178–21185.
- [23] C. E. A. Kirschhock, R. Ravishankar, P. A. Jacobs, J. A. Martens, J. Phys. Chem. B 1999, 103, 11021 – 11027.
- [24] C. E. A. Kirschhock, V. Buschmann, S. Kremer, R. Ravishankar, C. J. Y. Houssin, B. L. Mojet, R. A. van Santen, P. J. Grobet, P. A. Jacobs, J. A. Martens, *Angew. Chem. Int. Ed.* **2001**, *40*, 2637–2640; *Angew. Chem.* **2001**, *113*, 2707–2710.
- [25] C. E. A. Kirschhock, R. Ravishankar, L. V. Looveren, P. A. Jacobs, J. A. Martens, J. Phys. Chem. B 1999, 103, 4972 4978.
- [26] M. Song, K. Mitsuishi, K. Furuya, C. W. Allen, R. C. Birtcher, S. E. Donnelly, *Appl. Surf. Sci.* 2005, 241, 96–101.
- [27] a) D. P. Serrano, R. A. García, G. Vicente, M. Linares, D. Procházková, J. Čejka, J. Catal. 2011, 279, 366–380; b) K. A. Tarach, J. Tekla, W. Makowski, U. Filek, K. Mlekodaj, V. Girman, M. Choi, K. Góra-Marek, Catal. Sci. Technol. 2016, 6, 3568–3584.
- [28] R. Khare, D. Millar, A. Bhan, J. Catal. 2015, 321, 23-31.
- [29] a) S. Mitchell, A. B. Pinar, J. Kenvin, P. Crivelli, J. Kaerger, J. Perez-Ramirez, Nat. Commun. 2015, 6, 8633; b) D. Mores, J.

13967







- Kornatowski, U. Olsbye, B. M. Weckhuysen, Chem. Eur. J. 2011, 17, 2874-2884.
- [30] S. M. T. Almutairi, B. Mezari, E. A. Pidko, P. C. M. M. Magusin, E. J. M. Hensen, J. Catal. 2013, 307, 194-203.
- [31] a) S. Svelle, F. Joensen, J. Nerlov, U. Olsbye, K. P. Lillerud, S. Kolboe, M. Bjørgen, J. Am. Chem. Soc. 2006, 128, 14770 – 14771; b) X. Sun, S. Mueller, Y. Liu, H. Shi, G. L. Haller, M. Sanchez-Sanchez, A. C. van Veen, J. A. Lercher, J. Catal. 2014, 317, 185 – 197.
- [32] I. Yarulina, K. De Wispelaere, S. Bailleul, J. Goetze, M. Radersma, E. Abou-Hamad, I. Vollmer, M. Goesten, B. Mezari, E. J. M. Hensen, J. S. Martinez-Espin, M. Morten, S. Mitchell, J.
- Perez-Ramirez, U. Olsbye, B. M. Weckhuysen, V. Van Speybroeck, F. Kapteijn, J. Gascon, Nat. Chem. 2018, 10, 804-812.
- [33] S. Müller, Y. Liu, F. M. Kirchberger, M. Tonigold, M. Sanchez-Sanchez, J. A. Lercher, J. Am. Chem. Soc. 2016, 138, 15994-16003.
- [34] A. Comas-Vives, M. Valla, C. Coperet, P. Sautet, ACS Cent. Sci. **2015**, 1, 313 – 319.

Manuscript received: December 22, 2020 Revised manuscript received: March 29, 2021 Accepted manuscript online: April 12, 2021 Version of record online: May 17, 2021